Materials Horizons

ROYAL SOCIETY OF CHEMISTRY

COMMUNICATION

View Article Online
View Journal | View Issue



Check for updates

Cite this: *Mater. Horiz.*, 2024, 11, 4144

Received 3rd April 2024,
Accepted 6th June 2024

DOI: 10.1039/d4mh00377b

rsc.li/materials-horizons

# Performance of ferrite nanoparticles in inductive heating swing adsorption (IHSA): how tailoring material properties can circumvent the design limitations of a system†

Maxim De Belder, ‡[ac] Alysson F. Morais, ‡[ad] Natan De Vos,[a] Luc Van Meervelt,[b] Joeri F.M. Denayer,[c] Johan A. Martens[ad] and Eric Breynaert *[ad]

**Inductive heating swing adsorption (IHSA) using hybrid adsorbents incorporating a porous material and ferrite nanoparticles holds promise to be a performant, electrified alternative for conventional gas separation. Successful implementation of hybrid adsorbents in IHSA depends on achieving a maximal specific absorption rate (SAR) in the conditions and at the frequency of the induction setup. This paper outlines and demonstrates successful strategies for optimization of the particle composition, tailoring the coercivity and susceptibility of the ferrite particles to optimal performance in a given alternating magnetic field.**

**New concepts**

Ferrite susceptor materials are key to enabling efficient and environmentally sustainable gas separation processes. Where traditional temperature swing adsorption implements indirect and energy-inefficient flush gas heating, inductive heating swing adsorption (IHSA) operation directly transfers energy to adsorbent particles containing ferro/ferrimagnetic susceptor particles using an alternating magnetic field. In contrast with the classical industrial approach where an optimized process is designed in function of the properties of an optimized catalyst or adsorbent, induction heating infrastructure only allows minimal options for optimization of the magnitude and frequency of magnetic field driving the process. This work pioneers tailoring inductor material properties such as coercivity and magnetic susceptibility *via* chemical composition to maximize heating performance within the limits of real-world applications. Adopting a nuanced understanding of how the heat generation of realistic hysteresis loops is influenced by coercivity and magnetic susceptibility, this research provides insight into the design of performant IHSA systems.

## Introduction

Adsorption-based gas separation is a well-established unit operation in the chemical and petrochemical industries. It efficiently deals with a large range of separation needs including impurity removal, gas purification, and separation in recycle streams. The legislative outlook, enforcing a carbon-neutral industrial cycle by 2050,[1] empowers the call for increasing the efficiency of gas adsorption technologies, not only by developing new adsorbents with better separation characteristics but also by assisting process optimization. Especially in temperature swing adsorption processes (TSA), materials science can be an important driver.

Classically, the heat in a TSA process is supplied indirectly by using a pre-heated purge gas. Aside from being energy-inefficient, this operation exhibits inherent disadvantages. A conventional TSA process wastes over 41% of useful heat at the outlet. The purge gas, in addition, dilutes the end product, introducing additional processing requirements to upgrade or purify the output stream.[2,3]

By implementing ferro/ferrimagnetic hybrid adsorbents, inductive heating swing adsorption (IHSA) can assist in preventing these negative aspects. IHSA is fully electrified and transfers energy through space by applying a magnetic field that alternates at a frequency of Hz to kHz. This induces the ferro/ferrimagnetic components in the hybrid adsorbents to heat up, resulting in an *in situ* and targeted heating process which is isolated and thus energy efficient.

Inductive heating can be implemented using multiple mechanisms, including Joule heating (Eddy currents), heat generation *via* Brownian- and Néel relaxation, or heating *via* magnetic hysteresis losses.[4–6] In an industrial IHSA context,

[a] *Center for Surface Chemistry and Catalysis – Characterization and Application Team (COK-KAT), KU Leuven, 3001 Leuven, Belgium. E-mail: eric.breynaert@kuleuven.be*
[b] *Department of Chemistry, KU Leuven, 3001 Leuven, Belgium*
[c] *Department of Chemical Engineering, Vrije Universiteit Brussel, 1050 Brussels, Belgium*
[d] *NMRCoRe – NMR – X-Ray platform for Convergence Research, KU Leuven, 3001 Leuven, Belgium*

† Electronic supplementary information (ESI) available. See DOI: https://doi.org/10.1039/d4mh00377b

‡ These authors contributed equally to this work

only the latter offers a promising perspective (See clarification SI-1). Metallic susceptors, which use Eddy currents, are disregarded *a priori* as they suffer from long-term oxidative and chemical degradation. While Brownian and Néel relaxation are excellent mechanisms for heating nanoparticle suspensions, they do not apply to solid-state applications. Therefore, hysteresis losses emerge as the preferred mechanism for inductive heating in IHSA processes. Initial approaches to produce hybrid adsorbents suitable for IHSA using hysteresis losses embedded magnetite ($Fe_3O_4$) nanoparticles in zeolites or MOFs to trigger the adsorbate release *via* magnetic field cycling.[7,8] However, the use of magnetite as a susceptor material raises long-term stability concerns. The presence of $Fe^{2+}$ makes magnetite inherently prone to oxidation, detrimental to the inductive heating capabilities of the material. Spinel ferrite materials ($MFe_2O_4$; with $M^{2+}$ being a divalent cation such as $Mg^{2+}$, $Mn^{2+}$, $Co^{2+}$, $Ni^{2+}$, ...) offer a much more performant material, both in terms of heating potential as well as with respect to chemical stability. Unlike magnetite, ferrites are both oxidatively and thermally stable along with substantial chemical resistance.[9] They exhibit either a regular or inverse spinel crystal structure, incorporating one tetrahedral and two octahedral coordination sites in their lattice, as depicted in Fig. 1.[10] Their characteristic ferrimagnetic properties arise from the anti-parallel orientation of the magnetic moments of the octahedral sites with respect to the tetrahedral site.[11] Adjustment of the inductive heating properties of ferrites is easily achieved due to the large degree of synthetical flexibility. Besides magnetite, also ferrites have been implemented in an IHSA system (*e.g.* $MgFe_2O_4$ and $Cu_{0.2}Cd_{0.8}Fe_2O_4$ ferrites).[12,13] Yet the choice of susceptor material is never elaborated upon, nor purposefully rationalized. Instead, a purely empirical methodology in which available materials are tested within the design limitations of IHSA systems is the standard approach. Further advancements in the field of IHSA hinge on the tailoring of both susceptor materials and IHSA setups guided by general optimization principles.

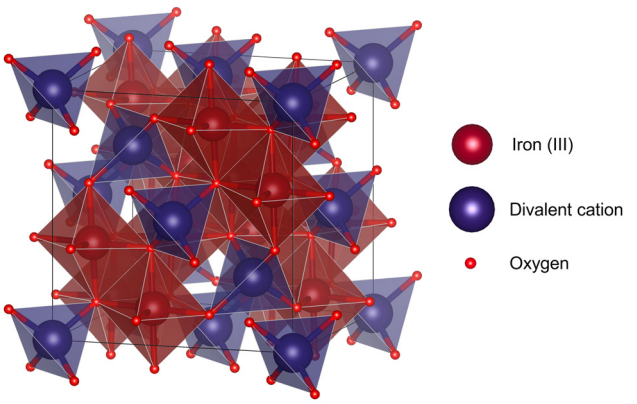


Fig. 1 Structure of a spinel ferrite. The red octahedrons represent the sites of $Fe^{3+}$. The blue tetrahedrons represent the sites of the divalent metal cations included in the spinel structure.

In this study, we outline a general strategy to guide the development of magnetic nanoparticles to be employed in IHSA systems. The magnetic hysteresis of these particles is modelled in terms of their coercivity ($H_C$), saturation magnetization ($M_S$) and normalized differential susceptibility ($\alpha$). The related hysteresis loss is calculated in terms of the maximum magnetic field achieved during the IHSA field cycling and optimization strategies aiming to increase the magnetic loss in these systems are discussed. The devised principles are experimentally illustrated and validated by the comparison of the heating properties of cobalt ferrite ($CoFe_2O_4$), cobalt-substituted nickel ferrites ($Ni_xCo_{1-x}Fe_2O_4$), and pure nickel ferrite ($NiFe_2O_4$), a series of materials whose coercivity, saturation magnetization and magnetic susceptibility can be modified by Ni(II) and Co(II) substitution in the ferrite structure.[13–17]

## Results & discussion

The choice of material has a profound influence on the performance of the inductive heating step in the IHSA cycle. Given the magnetization ($M$) curve of a susceptor material exposed to magnetic field ($H$) cycling, the amount of heat ($W$) that can be generated through hysteresis losses is directly proportional to the vacuum magnetic permeability ($\mu_0$) and the surface area enclosed by the hysteresis loop during a magnetization cycle:

$$W = \mu_0 \oint H \mathrm{d}M, \quad (1)$$

while the total power generated ($P$) is also linearly dependent upon the frequency ($f$) at which the applied field alternates:

$$P = Wf \quad (2)$$

Ferrite particles in a solid-state adsorbent are heated *via* magnetic hysteresis losses. A better heating performance is achieved by maximizing the surface area underneath the magnetic hysteresis loop (*cf.* eqn (1) and (2)). At first sight, such maximization could be achieved by increasing both the saturation magnetization and coercivity of the particles. However, deep saturation is hardly ever achieved in practical IHSA conditions. This naïve approach often leads to low IHSA performance. Based on only these principles, cobalt ferrite ($CoFe_2O_4$) would initially appear to be a suitable ferrite material for induction heating *via* magnetic hysteresis losses as it has a moderately high magnetization saturation ($M_S$ = 75 emu $g^{-1}$). Owing to its large magneto-crystalline anisotropy, it also exhibits a high coercivity ($H_C$ = 491 Oe).[14] In an experimental IHSA setup irradiated by an oscillatory magnetic field operating at 248 kHz with field strengths varying between 99 and 257 Oe, cobalt ferrite nanoparticles however do not provide a significant heat response (see Section S6, ESI†). Nickel ferrite nanoparticles in contrast perform much better at the same frequencies and field strengths, even though for the same particle size they feature much lower saturation magnetization ($M_S$ = 38 emu $g^{-1}$) and a much narrower magnetic hysteresis loop under saturation ($H_C$ = 29 Oe) as compared to cobalt ferrite

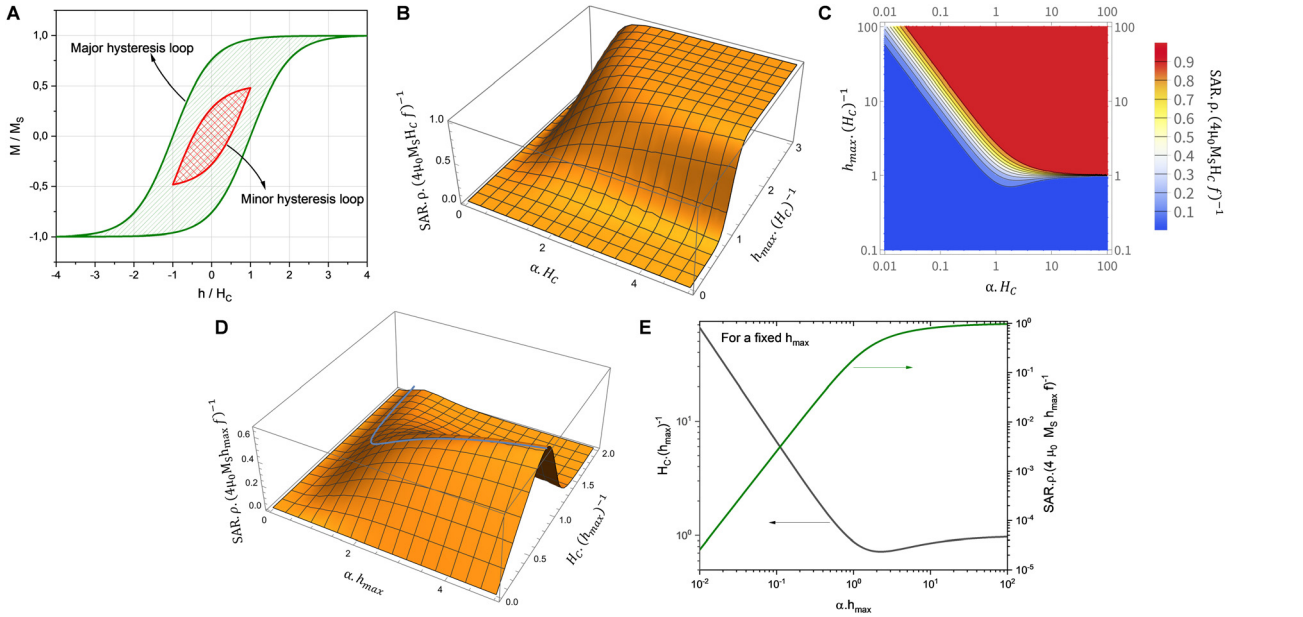


Fig. 2 (A) Representation of the major and a minor magnetic hysteresis loop for the same magnetic particles executed, respectively, when the particles are excited by a strong ($h_{max} \gg H_C$) and a weak ($h_{max} < \sim H_C$) magnetic field. (B) Modelled SAR (power generated per mass of susceptor material) as a function of $\alpha{\cdot}H_C$ and $h_{max}{\cdot}(H_C)^{-1}$. (C) Contour plot showing the contour lines of the surface in (B). (D) Modelled SAR as a function of $\alpha{\cdot}h_{max}$ and $H_C{\cdot}(h_{max})^{-1}$ and line representing the optimal condition where SAR is maximized for fixed magnetic field conditions ($h_{max}$ fixed). (E) Optimal condition shown by the line in (D). In the plots, $\rho$ represents the density of the susceptor material.

nanoparticles. These unexpected effects result from the shrunk, minor magnetic hysteresis loop executed by magnetic materials when magnetic saturation is not achieved during field cycling (see Fig. 2A).

The magnetic behaviour in minor hysteresis loops is dictated by the coercivity and the magnitude of the cycled magnetic field. Coercivity is a material property indicating the inherent resistance of a material against the realignment of spins in a field with opposite orientation. If this value is exceedingly high compared to the maximum excitation field strength ($h_{max}$), the magnetic moments are impeded from realigning with the swiftly alternating magnetic field (AMF). In this situation, only minor magnetic hysteresis loops are executed impacting the heat generation *via* hysteresis losses. It is then clear that for the design of efficient IHSA systems, a comprehensive optimization approach considering at the same time practical parameters such as excitation field strength ($h$) and materials properties such as coercivity, magnetic susceptibility and saturation magnetization ($M_S$) must be devised. Considering the simplest situation which implements minor hysteresis loops of single hyperbolic shape to illustrate the heating performance of ferrite nanoparticles in an IHSA setup, a simplified model describing the irreversible component ($M$) of the hysteresis loop as a single hyperbolic function is recovered:[15,16]

$$\frac{M}{M_S} = \begin{cases} \tan h[\alpha(h - H_C)] + b, h \text{ increasing up to } h_{max} \\ \tan h[\alpha(h + H_C)] - b, h \text{ decreasing up to } -h_{max} \end{cases} \quad (3)$$

with:

$$b = \frac{1}{2}[\tan h[\alpha(h_{max} + H_C)] - \tan h[\alpha(h_{max} - H_C)]] \quad (4)$$

In the limit when the magnetic field $h$ is cycled between $-\infty$ and $+\infty$, $b \rightarrow 0$ and the major magnetic hysteresis loop is recovered. In the case where deep saturation is not achieved, a minor hysteresis loop described by eqn (3) and (4) is executed, as depicted in Fig. 2A. The amount of heat generated by a magnetic system executing such a minor loop is dependent on $\alpha$, $H_C$ and $h_{max}$ (see Section S3, ESI†). To assist the visualisation of how these parameters impact the heat generated in an IHSA system, Fig. 2B and D show the hysteresis loss as a function of, respectively, the dimensionless parameters $\alpha H_C$ and $h_{max}/H_C$, and $\alpha h_{max}$ and $H_C/h_{max}$. These figures show that the heating capacity of the IHSA system can be maximized with a correct design of the coercivity and the magnetic susceptibility of the magnetic particles, as well as the excitation field.

To achieve an optimized heating, two strategies can be followed. Given a magnetic material ($\alpha$ and $H_C$ fixed), the first approach is to adjust the magnetic field conditions. This implies adjusting the field amplitude by tuning the current passed through the excitation coil. When soft magnetic particles ($\alpha{\cdot}H_C \ll 1$) are used in the IHSA system, the optimization of the system demands the application of magnetic fields with magnitude several times higher than the coercivity of the particles (see contour lines in Fig. 2C). To achieve 90% of the maximum possible heat generation, the optimization condition is given by $h_{max}(H_C)^{-1} = 2.4\ \alpha{\cdot}H_C$ or, equivalently, an optimized

 

magnetic field that is inversely proportional to the magnetic susceptibility of the particles:

$$h_{max} = \frac{2.39}{\alpha} \ (\text{for} \alpha \cdot H_C \ll 1) \quad (5)$$

Increasing the excitation field beyond this value still increases the heat generated in the IHSA system, but the gains are limited by the asymptotic behaviour of the SAR for high $h_{max}$, as observed in Fig. 2B.

As seen from Fig. 2B, the maximum possible SAR delivered by magnetic particles scales with their coercivity. Consequently, field optimization with the use of soft magnetic particles still intrinsically delivers IHSA systems with lower heating potential if compared to hard magnetic particles. With the use of hard magnetic particles ($\alpha \cdot H_C \gg 1$), hysteresis losses can be amplified. In this case, the optimization of the heat generated in the IHSA system demands matching the magnetic field to the coercivity of the particles:

$$h_{max} = H_C \quad (\text{for } \alpha \cdot H_C \gg 1) \quad (6)$$

Due to Ohmic losses in the feeding system, however, the window for tailoring the field conditions to the particle properties is limited, as increasing the current is detrimental to the overall efficiency of the heating process. In this case, the optimization of the IHSA system should also consider the technical trade-off between optimized heat and the overall energy losses in the system.

A second strategy to optimize the heat generation in the IHSA system is to adapt the magnetic particles to produce magnetic properties providing a better 'fit' with the magnetic field conditions. Fig. 2D shows that the heating performance of the IHSA system can be maximized with a correct design of the coercivity and the magnetic susceptibility of the magnetic particles. The optimization condition, illustrated in Fig. 2D by the blue line, is plotted in Fig. 2E. The optimal conditions can be expressed as:

$$H_C = \frac{0.67}{\alpha} \ (\text{for } \alpha \cdot h_{max} \ll 1) \quad (7)$$

$$H_C = h_{max} \quad (\text{for } \alpha \cdot h_{max} \gg 1) \quad (8)$$

Although eqn (7) and (8) can be useful rules of thumb to guide the design of an IHSA system, achieving such fully optimized situations demands fine control of the magnetic susceptibility and the coercivity of the magnetic particles at the same time. It is then more useful to consider the full picture depicted in Fig. 2D. Firstly, after maximizing the magnetic field delivered by the excitation coil according to the system's capability, the highest magnetic susceptibility should be sought, making the SAR to increase. However, while optimizing $\alpha$, care should be taken not to over tune the coercivity beyond the optimal expressed in eqn (7) and (8), which would lead SAR to quickly decrease, as shown by the steep decline of SAR in Fig. 2D beyond the optimal $H_C$.

To experimentally illustrate the devised principles, we compare the hysteresis loss of cobalt ferrite ($CoFe_2O_4$), cobalt-substituted nickel ferrites ($Ni_xCo_{1-x}Fe_2O_4$), and pure nickel ferrite ($NiFe_2O_4$) nanoparticles with the same particle size, as shown in Fig. 3. By replacing Co(II) by Ni(II) in $CoFe_2O_4$, the coercivity, the saturation magnetization and the magnetic susceptibility of the particles can be modified (see Table 1). To synthesise the particles, a co-precipitation approach similar to that used in the synthesis of layered double hydroxides was employed (see details in the ESI†). Soluble salts of the di- and tri-valent metals were added dropwise to a stirred, pH-controlled alkaline solution.[17,18] The resulting precipitate was subsequently aged and calcined. The obtained ferrites were characterized using TEM, PXRD and ICP-OES to confirm, respectively, their particle size, crystal structure and composition (see Fig. S1 and Table S1, S4, ESI†). SQUID magnetometry was used to obtain the magnetization curves of each sample (Table 1, Fig. 3 and Fig. S2–S4, ESI†). More details on the physicochemical characterization can be found in the ESI.† Alternative approaches for the synthesis of ferrites are thermal decomposition, sol–gel synthesis, and micro-emulsion synthesis.[19–23] Morphological parameters, such as size and shape, can be tailored by the choice of synthesis method and post-synthetic treatment.

Starting with an IHSA system employing $CoFe_2O_4$ nanoparticles and an excitation coil delivering $h_{max}$ = 99 Oe at 248 kHz, a SAR of 0.5 W $g^{-1}$ is obtained (see details on the measurement in the ESI†). The coercivity of such particles is well above the magnetic field delivered by the coil (see Table 1),

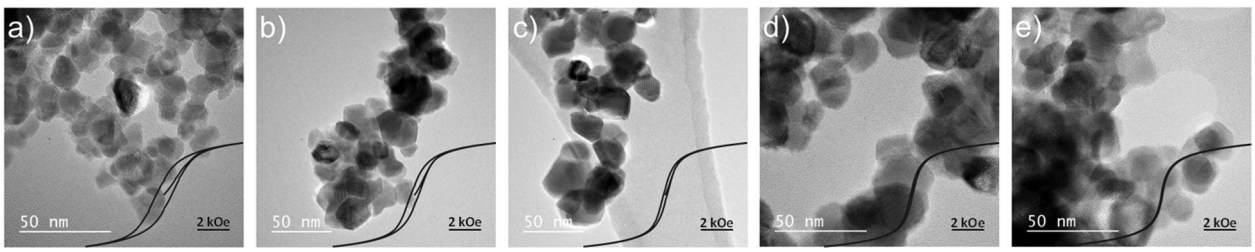


Fig. 3 TEM images of (a) CF, (b) NCF80, (c) NCF90, (d) NCF95, and (e) NF. The inset shows the magnetization curves (*M vs. H*) of each sample. The magnetization axis (*y*-axis) has been normalized by the saturation magnetization to facilitate comparison. Full magnetization curves are shown in Fig. S2 (ESI†). Please refer to Table 1 for details of sample composition and names.

Table 1 Ferrite samples with varying Ni(II) and Co(II) percentages

| Name | %Ni | %Co | $H_C$ (Oe) | $\alpha$ (1/kOe) | Formula |
|---|---|---|---|---|---|
| CF | 0 | 100 | 491 | 0.50 | $CoFe_2O_4$ |
| NCF 80 | 80 | 20 | 241 | 0.65 | $Ni_{0.80}Co_{0.20}Fe_2O_4$ |
| NCF 90 | 90 | 10 | 111 | 0.86 | $Ni_{0.90}Co_{0.10}Fe_2O_4$ |
| NCF 95 | 95 | 5 | 56.7 | 0.99 | $Ni_{0.95}Co_{0.05}Fe_2O_4$ |
| NF | 100 | 0 | 29.2 | 1.26 | $NiFe_2O_4$ |

thus leaving room for field optimization. In a first optimization step, the current in the excitation coil was increased up to the maximum permitted by the systems capabilities. In the maximum $h_{max}$ achieved (257 Oe), the SAR increased to 8.2 W $g^{-1}$ (see also Table S2, ESI†). As the coercivity of the $CoFe_2O_4$ particles is still higher than the achieved magnetic field, the composition of the particles was changed in a second optimization step. By decreasing the Co(II) content and increasing the Ni(II) content in $Ni_xCo_{1-x}Fe_2O_4$ ferrites, the coercivity can be granularly controlled and decreased down to $H_C$ = 29.2 Oe for pure-Ni ferrites. While the inclusion of Co(II) decreases the coercivity of the particles, it also increases the normalized differential susceptibility ($\alpha$) from 0.5 to 1.26 $kOe^{-1}$ (see Table 1). The hysteresis losses generated by the $Ni_xCo_{1-x}Fe_2O_4$ particles is shown in Fig. 4 for the six different values of $h_{max}$ employed: 99, 135.7, 158.3, 200.7, 226.2 and 257.3 Oe (see also Fig. S3, ESI†). By increasing $\alpha$ and decreasing $H_C$, the SAR at $h_{max}$ = 257 Oe was further improved to 43.8 W $g^{-1}$ ($NiFe_2O_4$ particles) even though the saturation magnetization of Ni-pure ferrites is two times lower than that of Co-pure ferrites (see Table S2, ESI†). This represents an increase of two orders of magnitude in the SAR as compared to the initial low $h_{max}$, low $\alpha$, high $H_C$ situation.

To assess the performance of the here presented $NiFe_2O_4$ ferrites against other ferrite systems, a compilation of selected ferrite materials reported elsewhere is provided as Table S3 in the ESI.† [12,13,24,25] To enable comparison, the SAR generated in one field cycle is considered, thus eliminating the influence of the different cycling frequencies employed in different applications (c.f. eqn (2)). The here reported NF ferrite ($NiFe_2O_4$) generates 177 mJ $g^{-1}$ of heat per field cycle in an optimized setup. The oxidation-prone pure-Fe ferrite magnetite, ($Fe_3O_4$, $H_C$ = 40 Oe, $M_S$ = 84 emu $g^{-1}$)[24] and Cu–Cd ferrite ($Cu_{0.2}Cd_{0.8}Fe_2O_4$, $H_C$ = 10 Oe, $M_S$ = 20 emu $g^{-1}$)[13] generate, respectively, 49.5 and 2.06 mJ $g^{-1}$ of heat in one field cycle in the reported experimental conditions. Comparing these materials readily demonstrates how much can be gained from a rational optimization approach embedded within the development and design of IHSA systems.

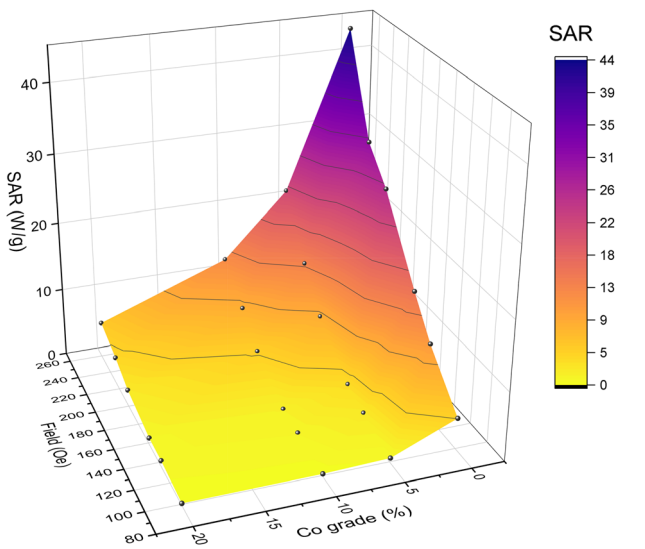


Fig. 4 SAR as a function of external field strength ($h_{max}$) and Co(II) substitution grade (excluding 100% Co(II)).

## Conclusion

Using an optimized ferrite susceptor material, inductive heating swing adsorption (IHSA) holds promise to become a performant technology alleviating the drawbacks of conventional thermal swing adsorption (TSA) processes. To ensure an energy-efficient heating performance, an optimization strategy is required considering the complex interplay between the amplitude of the induction field, the coercivity and susceptibility of the magnetic nanoparticles. In the design of an optimal IHSA system the magnetic field delivered by the excitation coil should be maximized according to the system's capability. Further optimization can be achieved by developing ferrite particles with high magnetic susceptibility and a coercivity tuned to the employed excitation field.

## Author contributions

M. De Belder: methodology, synthesis, characterization, and manuscript preparation. N. De Vos: synthesis. A. F. Morais: modelling, data interpretation, and manuscript preparation. L. Van Meervelt: characterization. All authors contributed to the writing of the manuscript. E. Breynaert conceived the project. E. Breynaert, J. A. Martens and J. Denayer contributed resources and supervised the project.

## Data availability

The data included in the figures are available free of charge in the KU Leuven institutional repository at **https://doi.org/10.48804/1LDRAQ**.

## Conflicts of interest

There are no conflicts to declare.

## Acknowledgements

J. A. M. acknowledges the Flemish Government for long-term structural funding (Methusalem). M. D. B., J. F. M. D., J. A. M., and E. B., acknowledge VLAIO for financial support in the

 

frame of the CAPTIN and CAPTIN-II moonshot projects (HBC.2021.0255). A. F. M. acknowledges support from the European Union's Horizon Europe programme through a Marie Skłodowska-Curie postdoctoral fellowship (No. 101063656, H2E). L. V. M. thanks the Hercules Foundation for supporting the purchase of the diffractometer through project AKUL/09/0035. NMRCoRe is supported by the Flemish Government as an international research infrastructure (I001321N: Nuclear Magnetic Resonance Spectroscopy Platform for Molecular Water Research) and acknowledges infrastructure support by Department EWI *via* the Hermes Fund (AH.2016.134) and by the Hercules Foundation (AKUL/13/21). This research was supported by the FWO infrastructure projects (AKUL13/19 and I000920N).

## Notes and references

1 European Commission, *Making the EU climate-neutral by 2050*, Brussels, 2020.
2 M. Clausse, J. Merel and F. Meunier, *Int. J. Greenhouse Gas Control*, 2011, **5**, 1206–1213.
3 A. Ntiamoah, J. Ling, P. Xiao, P. A. Webley and Y. Zhai, *Ind. Eng. Chem. Res.*, 2016, **55**, 703–713.
4 P. P. Vaishnava, R. Tackett, A. Dixit, C. Sudakar, R. Naik and G. Lawes, *J. Appl. Phys.*, 2007, **102**, 063914.
5 M. M. Sadiq, K. Suzuki and M. R. Hill, *Chem. Commun.*, 2018, **54**, 2825–2837.
6 J. E. Davies, *Conduction and induction heating*, Peter Peregrinus Ltd., London, 1990.
7 H. Li, M. M. Sadiq, K. Suzuki, R. Ricco, C. Doblin, A. J. Hill, S. Lim, P. Falcaro and M. R. Hill, *Adv. Mater.*, 2016, **28**, 1839–1844.
8 M. Gholami, B. Verougstraete, R. Vanoudenhoven, G. V. Baron, T. Van Assche and J. F. M. Denayer, *Chem. Eng. J.*, 2021, 133380.
9 A. V. Anupama, V. Kumaran and B. Sahoo, *Rheol. Acta*, 2019, **58**, 273–280.
10 K. E. Sickafus, J. M. Wills and N. W. Grimes, *J. Am. Ceram. Soc.*, 1999, **82**, 3279–3292.
11 L. Néel, *Proc. Phys. Soc., London, Sect. A*, 1952, **65**, 869.
12 M. M. Sadiq, H. Li, A. J. Hill, P. Falcaro, M. R. Hill and K. Suzuki, *Chem. Mater.*, 2016, **28**, 6219–6226.
13 R. Ghasemi, J. Echeverría, J. I. Pérez-Landazábal, J. J. Beato-Lopez, M. Naseri and C. Gómez-Polo, *J. Magn. Magn. Mater.*, 2020, **499**, 166201.
14 Z. Karimi, Y. Mohammadifar, H. Shokrollahi, S. K. Asl, G. Yousefi and L. Karimi, *J. Magn. Magn. Mater.*, 2014, **361**, 150–156.
15 J. Takacs, *Mathematics of Hysteretic Phenomena*, WILEY-VCH, Weinheim, 1st edn, 2003.
16 J. Takacs, G. Kovacs and L. K. Varga, *Eur. Phys. J.: Appl. Phys.*, 2010, **51**, 20801.
17 A. F. Morais, D. Nanclares, I. G. N. Silva, A. Duarte, F. A. Garcia, E. Breynaert and D. Mustafa, *Nanoscale*, 2021, **13**, 11781–11792.
18 A. F. Morais, I. G. N. Silva, B. J. Ferreira, A. C. Teixeira, S. P. Sree, H. Terraschke, F. A. Garcia, E. Breynaert and D. Mustafa, *Chem. Commun.*, 2023, **59**, 13571–13574.
19 P. A. Shaikh, R. C. Kambale, A. V. Rao and Y. D. Kolekar, *J. Alloys Compd.*, 2010, **492**, 590–596.
20 Q. Song, Y. Ding, Z. L. Wang and Z. J. Zhang, *Chem. Mater.*, 2007, **19**, 4633–4638.
21 R. Ali, M. A. Khan, A. Mahmood, A. H. Chughtai, A. Sultan, M. Shahid, M. Ishaq and M. F. Warsi, *Ceram. Int.*, 2014, **40**, 3841–3846.
22 D. H. Chen and X. R. He, *Mater. Res. Bull.*, 2001, **36**, 1369–1377.
23 A. Košak, D. Makovec, A. Žnidaršič and M. Drofenik, *J. Eur. Ceram. Soc.*, 2004, **24**, 959–962.
24 M. Bellusci, M. Albino, A. Masi, D. Peddis, C. Innocenti and F. Varsano, *Mater. Chem. Phys.*, 2024, **311**, 128525.
25 K. Newport, K. Baamran, A. A. Rownaghi and F. Rezaei, *Ind. Eng. Chem. Res.*, 2022, **61**, 18843–18853.